

# Homoepitaxial Growth of Large-Scale Highly Organized Transition Metal Dichalcogenide Patterns

Jianyi Chen, Xiaoxu Zhao, Gustavo Grinblat, Zhongxin Chen, Sherman J. R. Tan, Wei Fu, Zijing Ding, Ibrahim Abdelwahab, Yi Li, Dechao Geng, Yanpeng Liu, Kai Leng, Bo Liu, Wei Liu, Wei Tang, Stefan A. Maier, Stephen John Pennycook, and Kian Ping Loh\*

Controllable growth of highly crystalline transition metal dichalcogenide (TMD) patterns with regular morphology and unique edge structure is highly desired and important for fundamental research and potential applications. Here, single-crystalline MoS<sub>2</sub> flakes are reported with regular trigonal symmetric patterns that can be homoepitaxially grown on MoS<sub>2</sub> monolayer via chemical vapor deposition. The highly organized MoS<sub>2</sub> patterns are rhombohedral (3R)-stacked with the underlying MoS<sub>2</sub> monolayer, and their boundaries are predominantly terminated by zigzag Mo edge structure. The epitaxial MoS<sub>2</sub> crystals can be tailored from compact triangles to fractal flakes, and the pattern formation can be explained by the anisotropic growth rates of the S and Mo edges under low sulfur chemical potential. The 3R-stacked MoS<sub>2</sub> pattern demonstrates strong second and third-harmonic-generation signals, which exceed those reported for monolayer MoS<sub>2</sub> by a factor of 6 and 4, correspondingly. This homoepitaxial growth approach for making highly organized TMD patterns is also demonstrated for WS<sub>2</sub>.

TMDs permits the production of long-lived valley polarization by optical pumping.<sup>[4,5]</sup> In particular, noncentrosymmetric 3R-stacked TMDs provide a basis for the magnetic and electrical manipulation of spin/valley degrees of freedom.<sup>[6]</sup> Low-dimensional defects such as edges and grain boundaries also have unique structural properties due to their high level of dissymmetry.<sup>[7,8]</sup> In 2D materials, the presence of such defects can lead to interesting new properties such as tunable energy gap,<sup>[9]</sup> unusual magnetic correlations,<sup>[10]</sup> oscillating edge states,<sup>[11]</sup> high-performance nanoelectronics,<sup>[12]</sup> and edge nonlinear optics.<sup>[7]</sup> To be able to exploit these properties for applications, regular crystals with perfect stacking and well controlled unique edge structure,<sup>[5,13]</sup> have to be synthesized on a large scale. However, existing growth

Transition metal dichalcogenides (TMDs), MX<sub>2</sub> (M = Mo, W; X = S, Se, Te), have gained widespread interests due to their great potential in the fields of electronics, optoelectronics, and catalysis.<sup>[1–3]</sup> Broken inversion symmetry in

methods have limited control over the morphology and edge structures of TMD crystals.<sup>[14–17]</sup>

It is known that nonequilibrium growth processes can generate fractal patterns, these are exemplified in natural phenomena such as snowflakes.<sup>[18]</sup> The formation mechanism of these multi-branched structures is generally explained on the basis of diffusion-limited aggregation (DLA).<sup>[19]</sup> According to the DLA model, the strong binding of atoms limits adatom diffusion at low temperature, giving rise to fractal growth by an aggregation of hit-and-stick type.<sup>[20–22]</sup> The growth of 2D fractal patterns has not received the attention it deserves to date due to the challenge in controlling growth morphology, despite the advantage of possessing a high density of edge sites for catalytic applications. The question is whether a controllable self-organization mechanism exists for the large-scale growth of highly regular dendritic structures in 2D TMDs, where the macroscopic symmetry of the flakes can be tailored to replicate the microscopic symmetry of the crystals.

Here, we studied the homoepitaxial growth of MoS<sub>2</sub> crystals on the surface of MoS<sub>2</sub> monolayer. Under the condition of low S supply, the stark difference in growth rates between the different crystallographic edges promotes the rapid advancement of growth fronts of one polarity over the other, leading to nonequilibrium structures that are elongated at three sides. The homoepitaxially grown MoS<sub>2</sub> patterns are 3R-stacked with the underlying MoS<sub>2</sub> monolayer and terminated by zigzag Mo edges, as confirmed by high-resolution scanning transmission

Dr. J. Chen, X. Zhao, Z. Chen, S. J. R. Tan, Dr. W. Fu, Dr. Z. Ding, I. Abdelwahab, Dr. D. Geng, Dr. Y. Liu, K. Leng, Dr. B. Liu, Dr. W. Liu, Dr. W. Tang, Prof. K. P. Loh  
Graphene Research Centre and Department of Chemistry  
National University of Singapore  
6 Science Drive 2, Singapore 117546, Singapore  
E-mail: chmlhokp@nus.edu.sg

Dr. G. Grinblat, Dr. Y. Li, Prof. S. A. Maier  
The Blackett Laboratory  
Department of Physics  
Imperial College London  
London, SW7 2AZ, UK

Prof. S. A. Maier  
Chair in Hybrid Nanosystems  
Ludwig-Maximilians-Universität München  
München 80799, Germany

Prof. S. J. Pennycook  
Department of Materials Science & Engineering  
National University of Singapore  
Singapore 117575, Singapore

 The ORCID identification number(s) for the author(s) of this article can be found under <https://doi.org/10.1002/adma.201704674>.

DOI: 10.1002/adma.201704674

electron microscopy (STEM). Our growth recipe allows us to tune the shape of the crystals from triangular to fractal. The growth method is also applicable to other TMDs such as WS<sub>2</sub>, suggesting the generic applicability. In contrast to 2H-stacked bilayer and monolayer MoS<sub>2</sub>, the 3R-stacked MoS<sub>2</sub> patterns/monolayer system exhibits enhanced second and third harmonic generation (SHG and THG, respectively), suggesting that bilayer growth can be tailored for specific nonlinear optical applications.

**Figure 1** illustrates the procedure for the homoepitaxial growth of MoS<sub>2</sub> crystals. A piece of glass substrate used for growth was cleaned ultrasonically in acetone, isopropanol, and water, followed by 10 min of O<sub>2</sub> plasma, after which, it was placed on a piece of Mo foil. Another piece of curved Mo foil, used as the Mo source, was placed above the glass substrate. During the heating stage, a small quantity of ionic compounds present in the glass evaporates onto the surface of the Mo foil. Previous reports have shown that Na<sub>2</sub>O, NaCl, and SO<sub>2</sub>, among others, can corrode molybdenum metal by solid-state displacement reactions;<sup>[23–25]</sup> this helps with the volatilization of Mo. When the temperature at the center of the furnace approached 1050 °C, we moved the S source to set the temperature of S powders at 180 °C to grow MoS<sub>2</sub> crystals. The supply of Mo during growth is tuned by changing the distance between the Mo foil and the substrate (*h*), and the supply of S is controlled by its temperature. Due to the distinct catalytic behaviors of liquids,<sup>[26–28]</sup> large-sized MoS<sub>2</sub> monolayers were firstly grown on molten glass (Figure 1b,c). The large-area, highly uniform, and smooth MoS<sub>2</sub> monolayers are ideal templates to explore the homoepitaxial growth of MoS<sub>2</sub> crystals.

In our experiments, the homoepitaxial growth of MoS<sub>2</sub> crystals took place in the temperature range of 1030–1070 °C. The shape of the MoS<sub>2</sub> crystals can be tuned by controlling the ratio of S and Mo precursors. Keeping the temperature of S source at 230 °C and the distance *h* at 2 mm, small triangular-shaped MoS<sub>2</sub> crystals were grown on the surface of MoS<sub>2</sub> monolayer (Figure 1d). The regular triangular morphology with straight edges suggests that these crystals were grown under equilibrium condition. With decreasing S/Mo supply ratio, the population of the MoS<sub>2</sub> crystals decreases, and the size increases (Figure S1, Supporting Information). The edges of some crystals curl inward (Figure S1b, Supporting Information), suggesting a nonequilibrium growth process. As the supply of S is further reduced (180 °C), we observed the emergence of large-scale highly organized MoS<sub>2</sub> dendritic patterns on MoS<sub>2</sub> monolayer (Figure 1e). The width of the dendritic branches can be tuned by the distance *h* and growth time (Figures S2 and S3, Supporting Information), and adjacent branches merge to form a continuous film at long growth times (Figure S4, Supporting Information). Starting from a nucleation point, a MoS<sub>2</sub> flake has a three-level fractal structure (Figure 1f). The direction of these branches coincides with the armchair directions of MoS<sub>2</sub> crystals, and the angle between adjacent branches is about 60°. Figure 1g shows the size histogram of MoS<sub>2</sub> branches observed using optical microscopy. The largest branches have branch length of 650 μm. In addition, the uniform color contrast on MoS<sub>2</sub> monolayer indicates that these regular dendritic patterns are of uniform thickness.

To determine the structure of the MoS<sub>2</sub> patterns, the as-grown MoS<sub>2</sub> patterns/monolayer systems were transferred onto other substrates. The transferred sheets retained their structural

integrity (Figure 1h,i and Figure S5, Supporting Information). Atomic force microscopy (AFM) image of several MoS<sub>2</sub> branches is shown in Figure 1j. The observation showed that the grain directions of adjacent MoS<sub>2</sub> flakes are parallel to each other. The AFM line scan of a MoS<sub>2</sub> branch reveals a step height of ≈0.7 nm, which agrees well with the thickness of a MoS<sub>2</sub> monolayer.<sup>[15]</sup>

The atomic structure of the MoS<sub>2</sub> patterns was investigated by transmission electron microscopy (TEM). The TEM bright field image shown in **Figure 2a** reveals that parallel MoS<sub>2</sub> dendritic branches are grown on monolayer MoS<sub>2</sub>, as identified from the contrast highlighted by the white dashed line; these results are consistent with the optical microscopy and AFM observations. Selected-area electron diffraction (SAED) patterns recorded on both the MoS<sub>2</sub> monolayer and MoS<sub>2</sub> bilayer reveal that these regular flakes are single crystals (Figure 2b–d and Figure S6, Supporting Information). The presence of monolayer and bilayer domains was also identified by STEM–annular dark field (STEM–ADF) imaging (Figure 2e). Since the intensity of the ADF signal increases with atomic number, the Mo and S atoms as well as any possible superposition between them can be easily recognized from their relative intensities<sup>[29,30]</sup> (Figure 2f and Figure S7, Supporting Information). In Figure 2g, a magnified STEM–ADF image of a monolayer region is shown where bright spots correspond to Mo atoms and dim spots originate from two-stacked S atoms, revealing the trigonal prismatic geometry of the MoS<sub>2</sub> monolayer.<sup>[13]</sup> Interestingly, except for a minority of crystals, showing the 2H-phase (Figure S8, Supporting Information), the CVD-grown large patterns show a predominantly 3R-phase (space group R3m) (Figure 2h and Figure S9, Supporting Information), which are believed to be promoted by the high-temperature growth process.<sup>[13,31,32]</sup> The 3R-phase is AB-stacked with a staggered arrangement of Mo atoms over S atoms and has no inversion symmetry.<sup>[33]</sup> Figure 2i is a high-magnification STEM–ADF image taken near the edge of a MoS<sub>2</sub> flake; the corresponding atomic model is represented in Figure 2j. It is found that the edges of MoS<sub>2</sub> flakes follow the 1H crystal orientation and consist of Mo-zigzag edges, as highlighted by the blue dashed line.

X-ray photoelectron spectroscopy (XPS) was used to measure the binding energies of the MoS<sub>2</sub> patterns/monolayer system transferred on highly oriented pyrolytic graphite (HOPG). The peaks at ≈232.4 and 229.3 eV are attributed, respectively, to Mo 3d<sub>3/2</sub> and 3d<sub>5/2</sub> binding energies (Figure 3a), and the binding energies for S 2p<sub>1/2</sub> and S 2p<sub>3/2</sub> are located at 163.3 and 162.1 eV (Figure 3b), which is consistent with the reported values for MoS<sub>2</sub>.<sup>[34,35]</sup> Survey scan XPS spectrum (Figure 3c) reveals that the sample has high chemical purity, indicating that there are no external factors that will influence the growth of these highly regular MoS<sub>2</sub> patterns.

The optical properties of the MoS<sub>2</sub> patterns/monolayer system were characterized by Raman and PL spectroscopies using a 532 nm laser as the excitation source. Figure 3d–f, respectively, shows the optical image and corresponding Raman and PL spectra of trigonal symmetric MoS<sub>2</sub> patterns grown on MoS<sub>2</sub> monolayer. The Raman peaks at ≈404 and 385 cm<sup>-1</sup> are identified to be the A<sub>1g</sub> and E<sub>2g</sub> vibration modes of MoS<sub>2</sub> crystals (Figure 3d). The difference in peak frequencies between the A<sub>1g</sub> and E<sub>2g</sub> modes ( $\Delta$ ) can be used to identify the number of MoS<sub>2</sub> layers.<sup>[36,37]</sup> The value of  $\Delta$  for monolayer MoS<sub>2</sub> is ≈19.2 cm<sup>-1</sup>, while that for MoS<sub>2</sub> flake regions is 22.4 cm<sup>-1</sup>; this slight

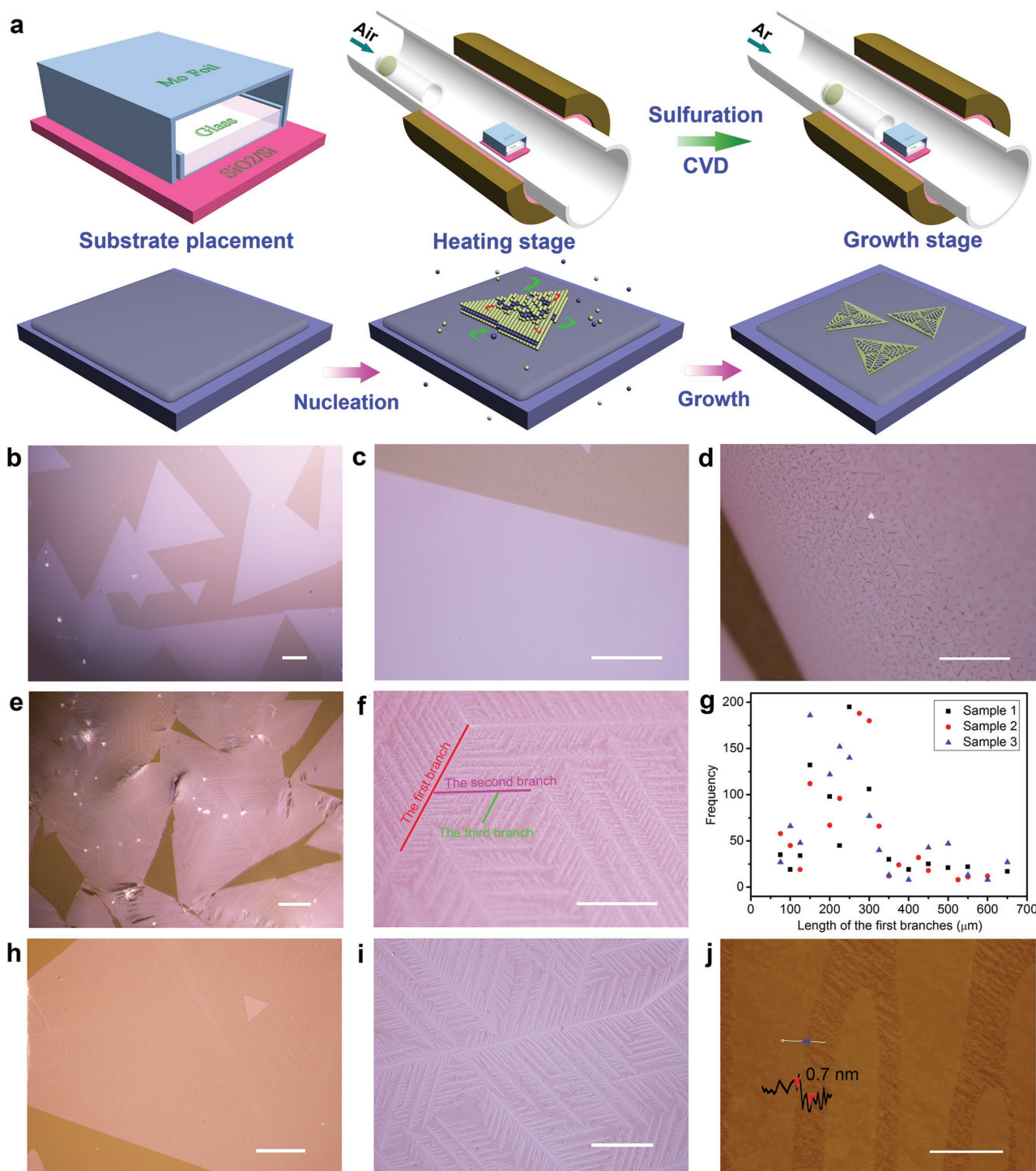


**Figure 1.** a) Scheme showing the CVD process for the homoepitaxial growth of highly organized MoS<sub>2</sub> dendritic patterns. b,c) Optical images of MoS<sub>2</sub> monolayer. Scale bar 200 μm in (b), and 50 μm in (c). d) Optical image of triangular MoS<sub>2</sub> crystals grown on MoS<sub>2</sub> monolayer; scale bar 50 μm. e) Optical image of regular MoS<sub>2</sub> dendritic patterns on the surface of MoS<sub>2</sub> monolayer. Scale bar 200 μm. f) High-magnification optical image of MoS<sub>2</sub> patterns. Scale bar 50 μm. g) Length distribution of the first branches based on three samples grown at same conditions. h,i) Optical images with different magnification of MoS<sub>2</sub> patterns/monolayer system transferred onto glass substrates. Scale bar is 100 μm in (h) and 50 μm in (i). j) AFM height image of MoS<sub>2</sub> flakes; scale bar 1 μm.

increase is consistent with the  $\Delta$  value for bilayers (Figure 3e). Figure 3f shows the PL spectrum of a MoS<sub>2</sub> monolayer domain with an emission peak at  $\approx 673$  nm corresponding to the direct

excitonic transition.<sup>[38]</sup> At the regular flake domains, a weaker PL peak is observed, similar to bilayer MoS<sub>2</sub>, where the inter-layer coupling changes the direct band gap into an indirect one.

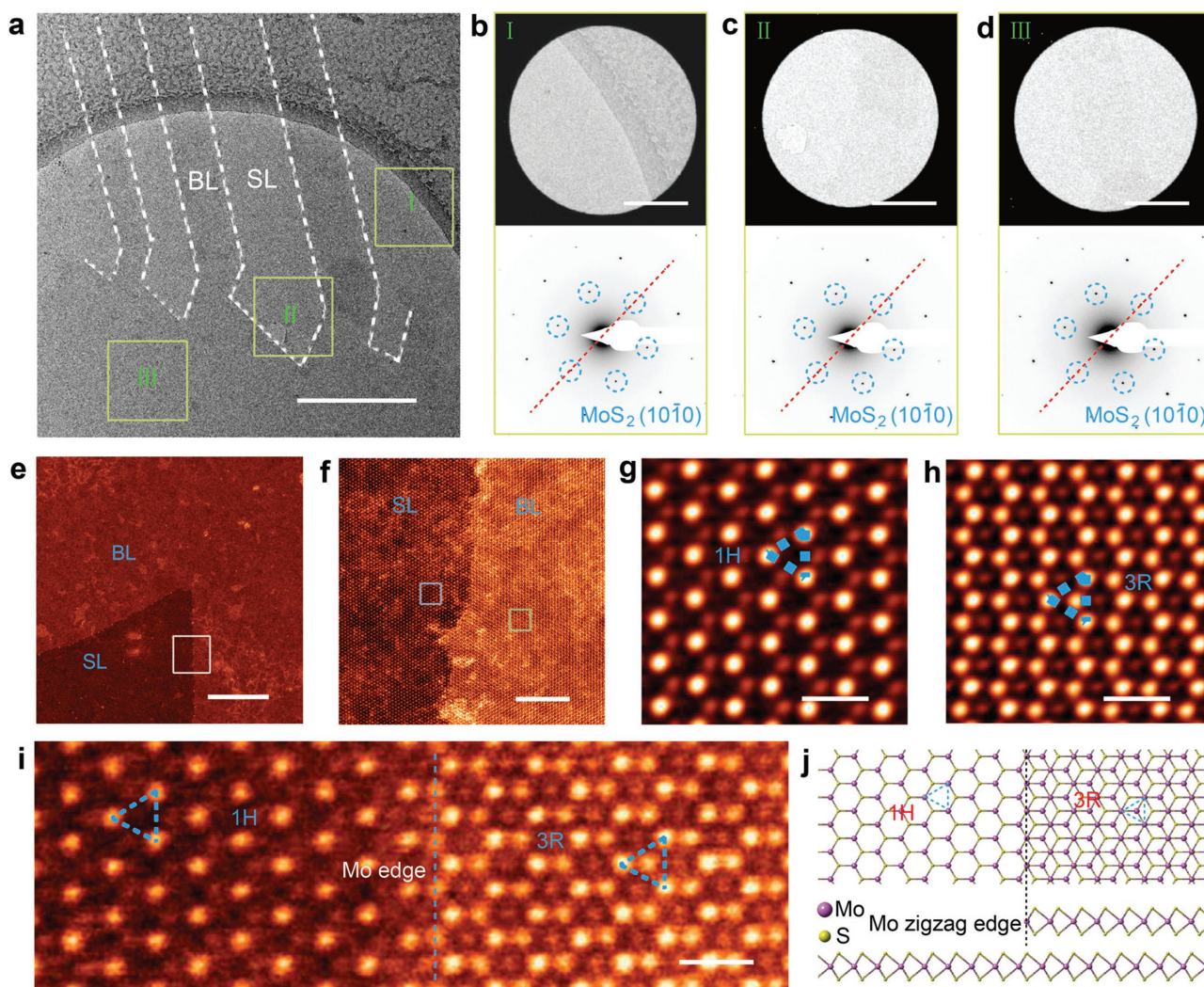


**Figure 2.** a) TEM bright-field image showing a typical flake region grown on single-layer (SL) MoS<sub>2</sub>; scale bar 500 nm. b–d) TEM bright-field images captured from the regions highlighted by yellow boxes in (a) and the corresponding SAED patterns revealing SL, SL + BL, and BL regions; scale bar 200 nm. e) STEM–ADF image of a typical region showing mono- and bilayer regions. Scale bar 200 nm. f) Magnified image of the region highlighted by a white box in (e) revealing a sharp Mo-zigzag edge. Scale bar 5 nm. g) Atomic STEM–ADF image of single-layer MoS<sub>2</sub> captured from regions in (f) shown by blue square box. Scale bar 0.5 nm. h) Atomic STEM–ADF image of bilayer MoS<sub>2</sub> captured from regions in (f) shown by the green square box. Scale bar 0.5 nm. i) Atomic STEM–ADF image depicting the 3R-phase with a Mo-zigzag edge. Scale bar 0.5 nm. j) Atomic model corresponding to the structure in (i) with cross-sectional view.

We also performed Raman and PL mappings of the region displayed in Figure 3d and compared their spatial profiles across regions with and without patterns (Figure 3g–i). The Raman and PL mapping signals correspond, respectively, to the integrated intensities of the characteristic MoS<sub>2</sub> Raman peak at the A<sub>1g</sub> mode (404 cm<sup>-1</sup>), the E<sub>2g</sub> mode (≈385 cm<sup>-1</sup>) and the PL emission centered at ≈673 nm. As expected, it is observed that the Raman intensity at the bilayer domains is higher than that at the monolayer domains, whereas the PL signal shows the opposite behavior due to the difference in bandgap behavior.

To assess the generality of our method, homoepitaxial growth of highly organized WS<sub>2</sub> patterns on WS<sub>2</sub> monolayer was studied using a similar strategy. WS<sub>2</sub> crystals were grown using W foil and S powders as the source precursors. Similar to the MoS<sub>2</sub> case, WS<sub>2</sub> flakes can also be grown on

WS<sub>2</sub> monolayer and the Raman and PL characterizations,<sup>[39]</sup> showing similar features for monolayer–bilayer system as in the MoS<sub>2</sub> case, are provided in Figures S10 and S11 in the Supporting Information.

The relative edge stability of the crystals is influenced by chemical potential of the growth precursors, and provides a strategy to tune the shape morphology of the crystals by controlling these factors. Figure 4a–c show the morphological evolution of our MoS<sub>2</sub> crystals grown on MoS<sub>2</sub> monolayer with different S supply. At high S supply, triangular MoS<sub>2</sub> crystals with three straight edges are formed (Figure 4a). When the S supply is lowered, the edges of the crystals curl inward (Figure 4b), and when the S supply is further lowered, highly symmetric flakes are formed (Figure 4c). We also observed some three-point star-shaped MoS<sub>2</sub> crystals (Figure 4d). The

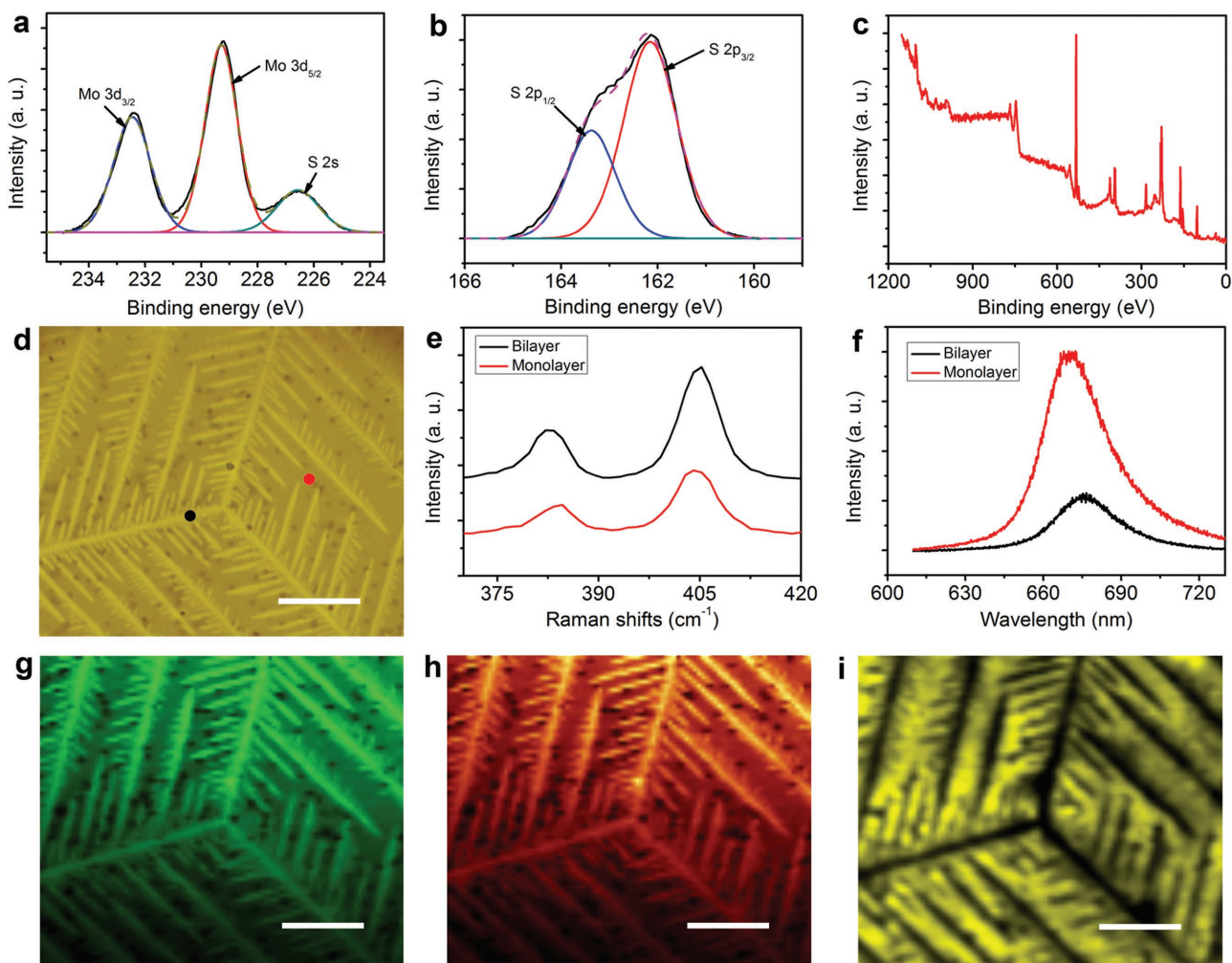


**Figure 3.** a–c) XPS spectra of MoS<sub>2</sub> dendritic patterns/monolayer system showing W 4f (a), S 2p (b), and survey spectrum (c). d) Optical image of trigonal symmetric MoS<sub>2</sub> patterns grown on MoS<sub>2</sub> monolayer. Scale bar 10  $\mu\text{m}$ . Raman spectra e) and PL f) of the underlying MoS<sub>2</sub> monolayer and the MoS<sub>2</sub> bilayer flakes labeled in (d). g,h) Raman spectroscopy maps of the peaks at  $\approx 385$  and  $404\text{ cm}^{-1}$ . Scale bar 10  $\mu\text{m}$ . i) PL spectroscopy map of the peak at 673 nm. Scale bar 10  $\mu\text{m}$ .

observed morphological change originates from the anisotropic growth rates of different edges, where the relative stability of the edge structures is different under different sulfur chemical potential  $\mu_S$ .<sup>[40]</sup> The formation energy ( $\gamma$ ) for four different types of edges (Figure 4e) varies with  $\mu_S$ , as shown in Figure 4f. It is known that under constant temperature and pressure, the chemical potentials of reactive elements are related to the relative composition. Therefore, a link between the theoretical formation energy of different edges and the controllable precursor amount can be built by  $\mu_S$ .

A ball-and-stick model showing a hexagonal-like cluster terminated by either the zigzag S edges and/or zigzag Mo edges, the two most common edges in CVD-grown crystal,<sup>[8]</sup> is illustrated in Figure 4g to explain how the relative stability of the edges affect the speed of propagation of the growth front. Figure 4h,i shows the interconversion of Mo and S-terminations at the zigzag Mo and zigzag S edges (marked in Figure 4g) during the propagation of the growth front; the process has different energy barriers depending on the edge type as well as

the chemical potential. Beginning from the zigzag S edges, the propagation of the growth front by one atomic row changes from the zigzag S edge to an antenna-Mo edge, and further extension reconverts it to a zigzag S edge (Figure 4h); the difference in formation energy between the antenna-Mo and the zigzag S edges is denoted by the energy barrier  $\Delta E_1$  (Figure 4f). When the growth starts at zigzag Mo edges, the edge changes from zigzag Mo edge to an antenna-S edge, and back to zigzag Mo edge with an energy barrier  $\Delta E_2$  (Figure 4i). The corresponding growth rates of zigzag S and zigzag Mo edges follow Arrhenius-type kinetics, accordingly the ratio between the edge growth rates is linked to the energy barriers of  $\Delta E_1$  and  $\Delta E_2$  at a constant  $\mu_S$

$$\frac{V_S}{V_{\text{Mo}}} = \exp\left[\frac{(\Delta E_2 - \Delta E_1)}{(\kappa_B T)}\right] \quad (1)$$

Because the values of  $\Delta E_1$  and  $\Delta E_2$  change with  $\mu_S$  (Figure 4j), the growth rates of the S and Mo edges can be adjusted by controlling the relative supply of S/Mo.

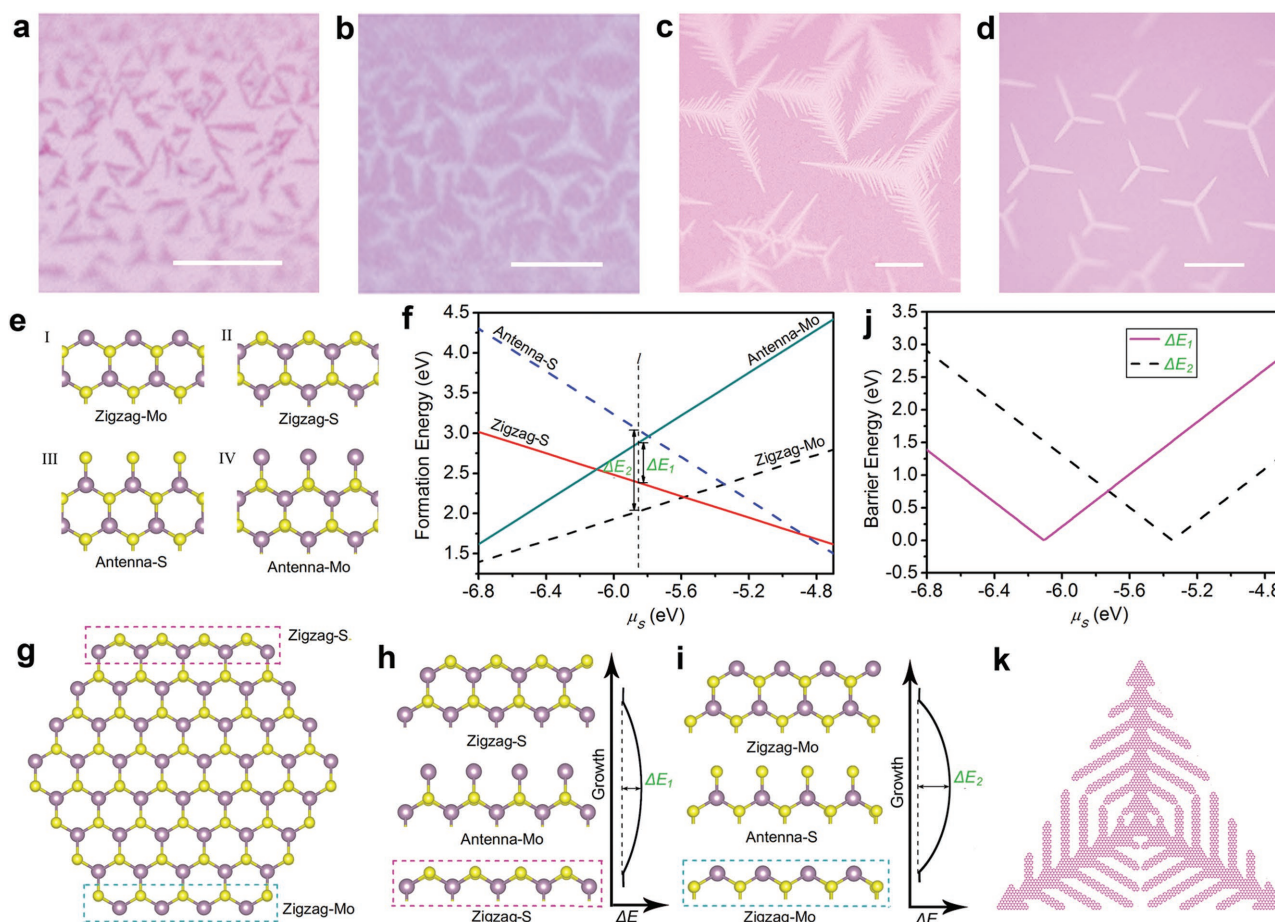


**Figure 4.** a–c) Optical images of dendritic MoS<sub>2</sub> crystals grown with different levels of S supply. Scale bar 10 μm in (a). Scale bar 10 μm in (b). Scale bar 100 μm in (c). d) Optical image of three-point star-like MoS<sub>2</sub> crystals. Scale bar 100 μm. e) Top view of the four different edge configurations of MoS<sub>2</sub> flakes. f) Variation of the edge formation energy with the chemical potential of sulfur  $\mu_s$  for the different edge configurations. g) Atomic ball model showing a MoS<sub>2</sub> hexagon exposing the two types of low-index edges, namely, zigzag S edges and zigzag Mo edges. h, i) Schematic views of how the zigzag S edge and the zigzag Mo edge change during a one-step growth with energy barriers of  $\Delta E_1$  and  $\Delta E_2$ , respectively. j) Variation of barrier energy of the S edges ( $\Delta E_1$ ) and Mo edges ( $\Delta E_2$ ) with the chemical potential of sulfur  $\mu_s$ , respectively. k) Schematic view of a regular dendritic crystal formed when  $v_s/v_{Mo}$  is  $\gg 2$ .

When the ratio of the edge growth rates ( $v_s/v_{Mo}$ ) is equal to 2 or 1/2 depending on the relative stability of the edge termination, the hexagonal-like cluster would grow into a triangular crystal (Figure 4a) with either three straight zigzag Mo edges or three zigzag S edges. However, if  $v_s/v_{Mo}$  is slightly  $>2$ , the growth rate of the zigzag Mo edges lags behind that of the zigzag S edges, and this will cause curved zigzag Mo edges to form (Figure 4b). Conversely, if  $v_s/v_{Mo}$  is slightly  $<1/2$ , the growth of the zigzag S edges lags behind that of the zigzag Mo edges and curved zigzag S edges are formed. Notably, when the supply of S (or  $\mu_s$ ) decreases further,  $\Delta E_1 \rightarrow 0$ , while  $\Delta E_2$  increases further (Figure 4j). This means that the growth of the zigzag Mo edges is increasingly inhibited by a large energy barrier, while the growth of the zigzag S edge would accelerate along three armchair directions (Figure 4d). As the size of the crystal increases, new zigzag S and zigzag Mo edges would form on both sides of the three main branches. After repeated nonequilibrium growth, the fast-growing S edge will grow itself into extinction and produce a highly organized MoS<sub>2</sub> pattern

terminated exclusively by zigzag Mo edges (Figure 4k and Figure S12, Supporting Information). The detailed mechanism of fractal growth still remains an active area of experimental and theoretical research, and further studies are underway in our laboratory.

Due to the alternation of monolayer 1H and bilayer 3R regions, the nonlinear optical characteristics of the homoepitaxially grown patterns should be spatially modulated. Therefore, we studied their SHG and THG responses using  $\lambda_{\text{pump}} = 1575$  nm excitation (Figure 5a). Probing the generation of harmonics helps to gain more information on the nonlinear optical susceptibility tensor of a material as well as on its structural symmetry.<sup>[41]</sup> Due to the breaking of inversion symmetry in monolayer 1H MoS<sub>2</sub>, it exhibits a strong SHG response as compared with bilayer 2H MoS<sub>2</sub>.<sup>[44]</sup> In contrast, since the THG response is described by a third-order process, it can occur irrespective of the number of layers. Figure 5b shows the corresponding SHG and THG spectra measured on a single MoS<sub>2</sub> branch, where two sharp peaks centered at

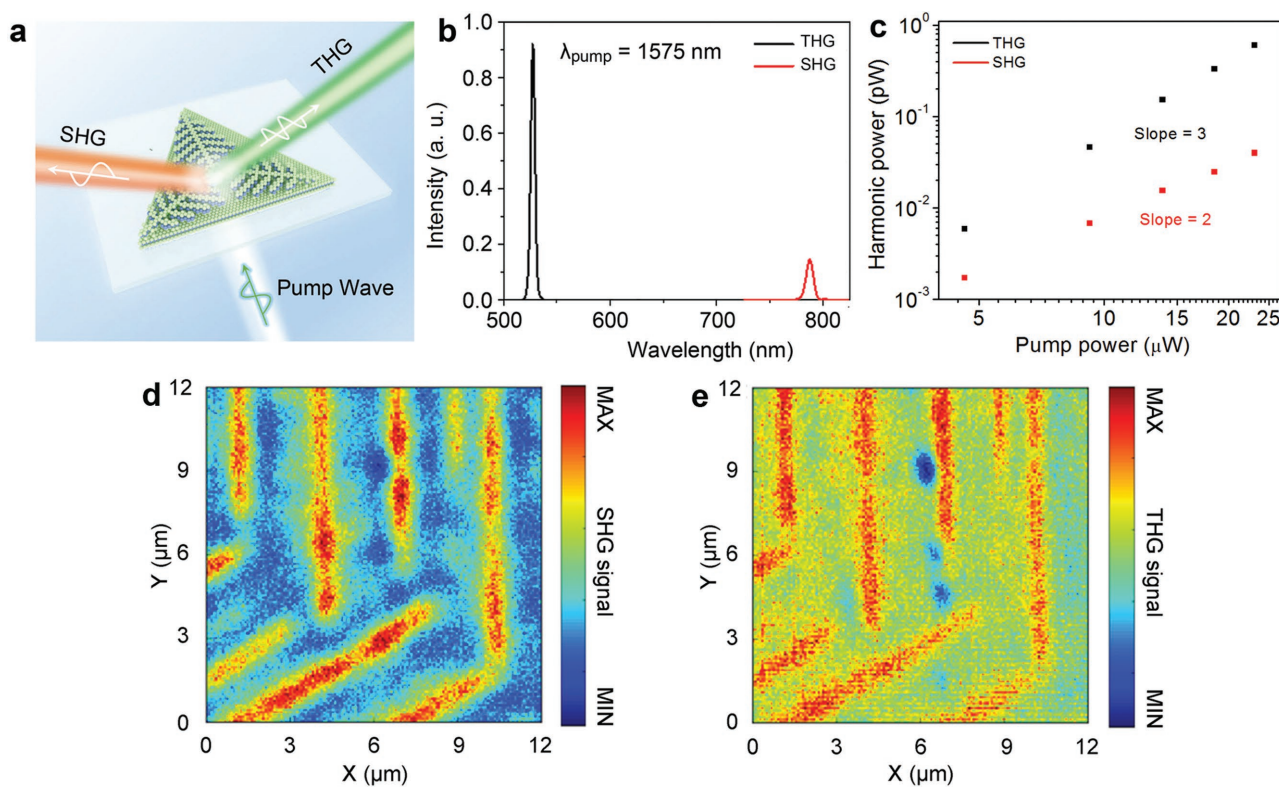


**Figure 5.** a) A schematic diagram illustrating the SHG and THG responses under excitation at  $\lambda_{\text{pump}} = 1575$  nm. b) SHG and THG spectra of the MoS<sub>2</sub> patterns/monolayer system excited at 1575 nm wavelength ( $\approx 1 \mu\text{m}^2$  spot size). c) Pump power dependence of the nonlinear signal for SHG (red) and THG (black) processes. d,e) Nonlinear spectral images acquired at the corresponding SHG and THG emission wavelengths.

$\lambda_{\text{pump}}/3$  (i.e., 525 nm) and  $\lambda_{\text{pump}}/2$  (787.5 nm) are observed. To quantify the associated second- and third-order nonlinear susceptibilities ( $\chi^{(2)}$  and  $\chi^{(3)}$ ), we measured the dependence of the SHG and THG signals on the pump power, as shown in Figure 5c. As expected, quadratic and cubic trends were found for the SHG and THG processes, respectively. By using the formulae relating  $\chi^{(2)}$  and  $\chi^{(3)}$  to pump and harmonic generation powers for a 2D material on a low-dispersion substrate, we obtain  $\chi^{(2)} = 4.8 \times 10^{-20} \text{ m}^2 \text{ V}^{-1}$  and  $\chi^{(3)} = 3.3 \times 10^{-28} \text{ m}^3 \text{ V}^{-2}$ . Remarkably, these values exceed those reported for monolayer MoS<sub>2</sub> (1H phase) by a factor of 2.4 and 2, correspondingly.<sup>[42]</sup> The nonlinear images acquired at the SHG and THG emission wavelengths reveal that the nonlinear signal is significantly larger at the MoS<sub>2</sub> patterns than at the monolayer regions, as shown in Figure 5d,e. Our results demonstrate that the SHG intensity in 3R-phase bilayer is considerably higher than that in the 2H-phase bilayer. This is due to the parallel alignment of dipoles between the layers, as opposed to antiparallel alignment in the case of the 2H samples.<sup>[43]</sup> Compared with stacked twisted bilayers by complicated transfer techniques,<sup>[44,45]</sup> the ability to produce large-scale 3R-stacking bilayer system should take us a step closer to real-world applications of TMDs. In addition, the highly organized MoS<sub>2</sub> patterns have high edge activity sites, making them efficient hydrogen evolution reaction (HER) electrocatalysts (Figure S13, Supporting Information).

In summary, hierarchically organized MoS<sub>2</sub> patterns were grown homoepitaxially on MoS<sub>2</sub> monolayer via CVD. The presence of large-scale 3R-stacked bilayer offers opportunities for

devices based on strong nonlinear optical response, and the high density of Mo-terminated edges can be exploited in catalysis. This study provides a route to fabricate TMDs in a hybrid monolayer–bilayer vertical structure, opening up opportunities for the engineering of TMD patterns for technological applications.

## Experimental Section

**Growth Procedure:** The homoepitaxial growth of highly organized MoS<sub>2</sub> patterns was achieved by using an ambient pressure CVD method. Glass substrates used for growth were cleaned ultrasonically in acetone (5 min), isopropanol (5 min), and water (5 min), followed by 10 min of O<sub>2</sub> plasma, after which, they were placed on a piece of Mo foil (0.05 mm thick, 99.95%). Another piece of curved Mo foil, used as the Mo source, was placed above the glass substrate. The glass substrates together with Mo foils were placed at the center of the hot zone in a furnace and heated to the desired temperature ( $\approx 1050$  °C). A quartz tube with one end sealed containing 0.8 g of S was located upstream, as an S source for the sulfuration of Mo. Ar gas (20 sccm) was used as the carrier gas. The furnace was heated to  $\approx 1050$  °C and stabilized for about 3 min, after which, S was introduced to the CVD, and maintained its temperature at  $\approx 180$  °C. After a growth period of 10 min, the furnace was cooled to room temperature quickly.

**Characterization:** AFM images were obtained using a Bruker Dimension FastScan Atomic Force Microscope in the tapping mode. TEM was performed with FEI Titan transmission electron microscope operated at 80 kV. STEM–ADF images were captured on an aberration-corrected JEOL ARM200F, equipped with a cold field emission gun, operating at 60 kV. Raman spectra were recorded at room temperature using a WITec Raman Microscope with laser excitation at 532 nm. XPS was carried out using SPECS XR-50 X-ray Mg K $\alpha$  (1253.7 eV) source with pass energy of

30 eV and spot size of 5 mm. The binding energy was determined by a PHOIBOS 150 hemispherical energy analyzer (SPECS, GmbH) equipped with a 3D delay line detector (3D-DLD, SPECS GmbH). The binding energies of the XPS spectra were calibrated to the Au  $4f_{7/2}$  peaks.

**Nonlinear Optical Measurement:** A pulsed Yb:KGW PHAROS laser system was used as the pump of a collinear optical parametric amplifier ORPHEUS with a LYRA wavelength extension option (Light Conversion Ltd, pulse duration of 180 fs, repetition rate of 100 kHz). The excitation beam ( $\lambda = 1575$  nm) was reflected by a shortpass dichroic mirror (Thorlabs DMSPI1000) and focused onto the sample with a 100 $\times$  (NA = 0.9) air objective from Nikon ( $\approx 1 \mu\text{m}^2$  spot size). The SHG/THG emission was collected in back-scattering configuration via the same objective and detected with an avalanche photodiode (MPD PDM Series by Picoquant) for imaging, or by a spectrograph (PI Acton SP2300 by Princeton Instruments) for spectral analysis. The sample was fixed to an XYZ piezo-scanner stage (Nano-Drive, Mad City Labs) during scanning. The power of the collected SHG/THG emission was measured with a calibrated silicon photodetector (Newport), while the excitation power was characterized with a germanium photodetector (Thorlabs).

## Supporting Information

Supporting Information is available from the Wiley Online Library or from the author.

## Acknowledgements

J.C. and X.Z. contributed equally to this work. J.C. conceived the idea and wrote the paper. K.P.L. and J.C. acknowledge support by the National Research Foundation, Singapore, Mid-sized Centre grant (CA2DM) under the Prime Minister's Office. S.A.M., G.G. and Y.L. acknowledge the EPSRC Reactive Programme EP/M013812/1. G.G. further acknowledges a Marie Skłodowska-Curie fellowship.

## Conflict of Interest

The authors declare no conflict of interest.

## Keywords

2D materials, chemical vapor deposition, harmonic generation, highly organized patterns, homoepitaxial growth, transition metal dichalcogenides

Received: August 16, 2017

Revised: September 14, 2017

Published online: December 8, 2017

- [1] Q. H. Wang, K. Kalantar-Zadeh, A. Kis, J. N. Coleman, M. S. Strano, *Nat. Nanotechnol.* **2012**, *7*, 699.
- [2] X. Duan, C. Wang, J. C. Shaw, R. Cheng, Y. Chen, H. Li, X. Wu, Y. Tang, Q. Zhang, A. Pan, J. Jiang, R. Yu, Y. Huang, X. Duan, *Nat. Nanotechnol.* **2014**, *9*, 1024.
- [3] R. Lv, J. A. Robinson, R. E. Schaak, D. Sun, Y. Sun, T. E. Mallouk, M. Terrones, *Acc. Chem. Res.* **2015**, *48*, 56.
- [4] H. Zeng, J. Dai, W. Yao, D. Xiao, X. Cui, *Nat. Nanotechnol.* **2012**, *7*, 490.
- [5] K. F. Mak, K. He, J. Shan, T. F. Heinz, *Nat. Nanotechnol.* **2012**, *7*, 494.
- [6] R. Suzuki, M. Sakano, R. Y. J. Zhang, A. D. Morikawa, A. Harasawa, K. Yaji, K. Kuroda, K. Miyamoto, T. Okuda, K. Ishizaka, R. Arita, Y. Iwasa, *Nat. Nanotechnol.* **2014**, *9*, 611.
- [7] X. Yin, Z. Ye, D. A. Chenet, Y. Ye, K. O'Brien, J. C. Hone, X. Zhang, *Science* **2014**, *344*, 488.
- [8] A. M. van der Zande, P. Y. Huang, D. A. Chenet, T. C. Berkelbach, Y. You, G. -H. Lee, T. F. Heinz, D. R. Reichman, D. A. Muller, J. C. Hone, *Nat. Mater.* **2013**, *12*, 554.
- [9] Y. -W. Son, M. L. Cohen, S. G. Louie, *Phys. Rev. Lett.* **2006**, *97*, 216803.
- [10] O. V. Yazyev, M. I. Katsnelson, *Phys. Rev. Lett.* **2008**, *100*, 047209.
- [11] H. Xu, S. Liu, Z. Ding, S. J. R. Tan, K. M. Yam, Y. Bao, C. T. Nai, M. -F. Ng, J. Lu, C. Zhang, K. P. Loh, *Nat. Commun.* **2016**, *7*, 12904.
- [12] T. F. Jaramillo, K. P. Jørgensen, J. Bonde, J. H. Nielsen, S. Horch, I. Chorkendorff, *Science* **2007**, *317*, 100.
- [13] M. Chhowalla, H. S. Shin, G. Eda, L.-J. Li, K. P. Loh, H. Zhang, *Nat. Chem.* **2013**, *5*, 263.
- [14] S. Najmaei, Z. Liu, W. Zhou, X. Zou, G. Shi, S. Lei, B. I. Yakobson, J. -C. Idrobo, P. M. Ajayan, J. Lou, *Nat. Mater.* **2013**, *12*, 754.
- [15] Y.-H. Lee, X.-Q. Zhang, W. Zhang, M.-T. Chang, C.-T. Lin, K.-D. Chang, Y.-C. Yu, J. T.-W. Wang, C.-S. Chang, L.-J. Li, T.-W. Lin, *Adv. Mater.* **2012**, *24*, 2320.
- [16] X. Wang, H. Feng, Y. Wu, L. Jiao, *J. Am. Chem. Soc.* **2013**, *135*, 5304.
- [17] J. Chen, B. Liu, Y. Liu, W. Tang, C. T. Nai, L. Li, J. Zheng, L. Gao, Y. Zheng, H. S. Shin, H. Y. Jeong, K. P. Loh, *Adv. Mater.* **2015**, *27*, 6722.
- [18] S. Tolansky, *Nature* **1958**, *181*, 256.
- [19] T. A. Witten, L. M. Sander, *Phys. Rev. Lett.* **1981**, *47*, 1400.
- [20] M. Einax, *Rev. Mod. Phys.* **2013**, *85*, 921.
- [21] H. Roder, K. Bromann, H. Brune, K. Kern, *Phys. Rev. Lett.* **1995**, *74*, 3217.
- [22] Y. Zhang, Q. Ji, G. -F. Han, J. Ju, J. Shi, D. Ma, J. Sun, Y. Zhang, M. Li, X. -Y. Lang, Y. Zhang, Z. Liu, *ACS Nano* **2014**, *8*, 8617.
- [23] V. V. Karpov, A. V. Abramov, A. Y. Zhilyakov, S. V. Belikov, V. A. Volkovich, I. B. Polovov, O. I. Rebrin, *AIP Conf. Proc.* **2016**, *1767*, 020011.
- [24] M. Farber, D. M. Ehrenberg, *J. Electrochem. Soc.* **1952**, *99*, 427.
- [25] J. Liu, L. Lei, Y. Wang, G. Wu, Z. Wu, *Phys. Chem. Glasses: Eur. J. Glass Sci. Technol., Part B* **2015**, *56*, 212.
- [26] D. Geng, B. Wu, Y. Guo, L. Huang, Y. Xue, J. Chen, G. Yu, L. Jiang, W. Hu, Y. Liu, *Proc. Natl. Acad. Sci. USA* **2012**, *109*, 7992.
- [27] B. Wu, D. Geng, Z. Xu, Y. Guo, L. Huang, Y. Xue, J. Chen, G. Yu, Y. Liu, *NPG Asia Mater.* **2013**, *5*, e36.
- [28] Y. Chen, J. Sun, J. Gao, F. Du, Q. Han, Y. Nie, Z. Chen, A. Bachmatiuk, M. K. Priyadarshi, D. Ma, X. Song, X. Wu, C. Xiong, M. H. Rummeli, F. Ding, Y. Zhang, Z. Liu, *Adv. Mater.* **2015**, *27*, 7839.
- [29] J. Chen, X. Zhao, S. J. Tan, H. Xu, B. Wu, B. Liu, D. Fu, W. Fu, D. Geng, Y. Liu, W. Liu, W. Tang, L. Li, W. Zhou, T. C. Sum, K. P. Loh, *J. Am. Chem. Soc.* **2017**, *139*, 1073.
- [30] M.-Y. Li, Y. Shi, C.-C. Cheng, L.-S. Lu, Y.-C. Lin, H.-L. Tang, M.-L. Tsai, C.-W. Chu, K.-H. Wei, J.-H. He, W.-H. Chang, K. Suenaga, L.-J. Li, *Science* **2015**, *349*, 524.
- [31] S. Wang, J. Zhang, D. He, Y. Zhang, L. Wang, H. Xu, X. Wen, H. Ge, Y. Zhao, *J. Phys. Chem. Solids* **2014**, *75*, 100.
- [32] J. Shi, P. Yu, F. Liu, P. He, R. Wang, L. Qin, J. Zhou, X. Li, J. Zhou, X. Sui, S. Zhang, Y. Zhang, Q. Zhang, T. C. Sum, X. Qiu, Z. Liu, X. Liu, *Adv. Mater.* **2017**, *29*, 1701486.
- [33] A. Yan, W. Chen, C. Ophus, J. Ciston, Y. Lin, K. Persson, A. Zettl, *Phys. Rev. B* **2016**, *93*, 041420 (R).
- [34] J. Chen, W. Tang, B. Tian, B. Liu, X. Zhao, Y. Liu, T. Ren, W. Liu, D. Geng, H. Y. Jeong, H. S. Shin, W. Zhou, K. P. Loh, *Adv. Sci.* **2016**, *3*, 1500033.
- [35] G. Tai, T. Zeng, J. Yu, J. Zhou, Y. You, X. Wang, H. Wu, X. Sun, T. Hu, W. Guo, *Nanoscale* **2016**, *8*, 2234.

- [36] C. Lee, H. Yan, L. E. Brus, T. F. Heinz, J. Hone, S. Ryu, *ACS Nano* **2010**, *4*, 2695.
- [37] Y. Zhan, Z. Liu, S. Najmaei, P. M. Ajayan, J. Lou, *Small* **2012**, *8*, 966.
- [38] A. Splendiani, L. Sun, Y. Zhang, T. Li, J. Kim, C. -Y. Chim, G. Galli, F. Wang, *Nano Lett.* **2010**, *10*, 1271.
- [39] J. Chen, W. Zhou, W. Tang, B. Tian, X. Zhao, H. Xu, Y. Liu, D. Geng, S. J. R. Tan, W. Fu, K. P. Loh, *Chem. Mater.* **2016**, *28*, 7194.
- [40] S. Zhu, Q. Wang, *AIP Adv.* **2015**, *5*, 107105.
- [41] L. Zhang, K. Liu, A. B. Wong, J. Kim, X. Hong, C. Liu, T. Cao, S. G. Louie, F. Wang, P. Yang, *Nano Lett.* **2014**, *14*, 6418.
- [42] R. I. Woodward, R. T. Murray, C. F. Phelan, R. E. P. de Oliveira, T. H. Runcorn, E. J. R. Kelleher, S. Li, E. C. de Oliveira, G. J. M. Fechine, G. Eda, C. J. S. de Matos, *2D Mater.* **2017**, *4*, 011006.
- [43] Y. Li, Y. Rao, K. F. Mak, Y. You, S. Wang, C. R. Dean, T. F. Heinz, *Nano Lett.* **2013**, *13*, 3329.
- [44] W.-T. Hsu, *ACS Nano* **2014**, *8*, 2951.
- [45] A. M. van der Zande, J. Kunstmann, A. Chernikov, D. A. Chenet, Y. You, X. Zhang, P. Y. Huang, T. C. Berkelbach, L. Wang, F. Zhang, M. S. Hybertsen, D. A. Muller, D. R. Reichman, T. F. Heinz, J. C. Hone, *Nano Lett.* **2014**, *14*, 3869.